The Astrophysical Journal, 984:130 (8pp), 2025 May 9 https://doi.org/10.3847/1538-4357/adc98f

A Phase-resolved View of Millihertz Quasiperiodic Oscillations in the Ultraluminous X-Ray Source M51 ULX-7: Evidence for a Magnetically Truncated Disk and Geometrical Beaming

Qing-Cang Shui[1,2], Shu Zhang[1], Hua Feng[1], Yu-Peng Chen[1], Shuang-Nan Zhang[1,2], and Jing-Qiang Peng[1,2]
[1] Key Laboratory of Particle Astrophysics, Institute of High Energy Physics, Chinese Academy of Sciences, 100049 Beijing, People's Republic of China; szhang@ihep.ac.cn, hfeng@ihep.ac.cn
[2] University of Chinese Academy of Sciences, Chinese Academy of Sciences, 100049 Beijing, People's Republic of China
Received 2025 January 8; revised 2025 April 2; accepted 2025 April 4; published 2025 May 6

Abstract

X-ray quasiperiodic oscillations (QPOs) are commonly observed in Galactic X-ray binaries and extragalactic ultraluminous X-ray sources (ULXs). In this study, we perform a phase-resolved analysis of recently discovered X-ray mHz QPOs in M51 ULX-7. This represents the first detailed phase-resolved analysis of QPOs conducted in ULXs. Our findings reveal that the amplitude of the mHz QPO slightly increases with photon energy, accompanied by a narrowing of the phase modulation profile. The phase-resolved spectroscopy indicates significant variability in the energy spectrum: both disk blackbody components exhibit marked variations on the QPO timescale, with the low-temperature component demonstrating significant synchronous changes in the disk temperature and luminosity, showing a positive correlation between these two parameters throughout the QPO cycle. This correlation supports the hypothesis that the disk inner radius corresponds to the magnetospheric radius, which slightly varies with the accretion rate. Our results suggest that the soft component, without beaming, originates from a magnetically truncated outer disk, while the hard component is geometrically beamed from the inner funnel regions.

Unified Astronomy Thesaurus concepts: Accretion (14); Neutron stars (1108); Pulsars (1306); Ultraluminous x-ray sources (2164)

1. Introduction

Ultraluminous X-ray sources (ULXs) are off-nuclear, point-like, bright X-ray sources with apparent luminosities exceeding $\sim 10^{39}\,\mathrm{erg\,s^{-1}}$, which result from accretion onto a compact object (see H. Feng & R. Soria 2011, P. Kaaret et al. 2017, and A. King et al. 2023 for comprehensive reviews). The remarkable detection of coherent pulsations in M82 ULX-2 (M. Bachetti et al. 2014) demonstrated that ULXs can be powered by magnetic neutron stars (NSs), leading to the classification of these sources as pulsating ULXs (PULXs). To date, among more than 1800 identified ULXs, there are six known extragalactic PULXs, most of which emit at super-Eddington luminosities (D. J. Walton et al. 2022; H. Tranin et al. 2024).

The discovery of these PULXs marks a significant milestone that poses a challenge to the current understanding of both ULXs and the magnetospheric accretion of NSs (see, e.g., A. A. Mushtukov et al. 2017). PULXs are considered to be driven by NSs with extremely high mass accretion rates and/or exceptionally strong magnetic fields. At such extreme mass accretion rates, geometrically thick, radiation-pressure-dominated accretion disks are expected to produce strong outflows (N. I. Shakura & R. A. Sunyaev 1973; G. V. Lipunova 1999; J. Poutanen et al. 2007), which have been observed in both simulations and observations of several sources (see, e.g., K. Ohsuga & S. Mineshige 2011; Y.-F. Jiang et al. 2014; C. Pinto et al. 2016; P. Kosec et al. 2018a, 2018b; C. Pinto et al. 2020). These outflows may be optically thick and form a funnel-like structure, which plays an important role in shaping emergent X-ray energy spectrum and timing behaviors. For instance, beaming of X-ray emission from the funnel is expected. This beaming affects the apparent luminosity $L_{\rm app}$, enhancing it relative to the accretion luminosity L by a factor of b^{-1}. The determination of the beaming factor b remains a subject of debate. Some studies assumed b to be close to unity (see, e.g., S. Dall'Osso et al. 2015; A. A. Mushtukov et al. 2017, 2019, 2021), while others proposed a relatively higher beaming factor with $b^{-1} \gtrsim 20$ (see, e.g., A. King et al. 2017; M. J. Middleton & A. King 2017).

Investigating short-term variability can impose constraints on different accretion models in ULXs (see, e.g., D. R. Pasham et al. 2014). Specifically, quasiperiodic oscillations (QPOs) have been detected in the frequency range of ~0.5–600 mHz in a few ULXs (e.g., M82 X-1, Holmberg IX X-1, NGC 5408 X-1, NGC 6946 X-1, M82 X-2, IC 342 X-1, 4XMM J140314.2+541806, and M51 ULX-7; T. E. Strohmayer & R. F. Mushotzky 2003; G. C. Dewangan et al. 2006; T. E. Strohmayer et al. 2007; F. Rao et al. 2010; H. Feng et al. 2010; V. K. Agrawal & A. Nandi 2015; R. T. Urquhart et al. 2022; M. Imbrogno et al. 2024). The origin of QPOs in X-ray binaries (XRBs), and especially in ULXs, remains a topic of debate, with several alternative explanations proposed (see A. R. Ingram & S. E. Motta 2019 for a review). The mHz frequency range is too low to align with Keplerian rotation in the region responsible for X-ray emission. Instead, these frequencies might be associated with the Lense–Thirring precession of inflows/outflows (M. J. Middleton et al. 2018, 2019). Additionally, another form of quasiperiodic variability is observed at frequencies around 1 mHz in the ULX 4XMM J111816.0–324910 (S. E. Motta et al. 2020), which resembles the so-called "heartbeat" variability typically seen in the Galactic black hole XRB GRS 1915+105 (T. Belloni et al. 2000). This "heartbeat" variability has often been interpreted as limit-cycle instabilities

Table 1
Log of XMM-Newton Observations of M51 Used in This Work

#	Observation ID	Start Time (MJD)	Exposure Time[a] (ks)
1	0883550101	59540.40	130.4
2	0883550201	59542.39	130.2
3	0883550301	59586.25	131.4

Note.
[a] Preflare filtering exposure time.

within the inner accretion disk, likely arising from radiation pressure instability (A. P. Lightman & D. M. Eardley 1974; E. Szuszkiewicz & J. C. Miller 1998; A. Janiuk et al. 2000; S. Nayakshin et al. 2000).

M51 consists of an interacting galaxy pair, which includes the active, face-on spiral galaxy NGC 5194 and its companion, the dwarf galaxy NGC 5195. The X-ray source known as M51 ULX-7 (hereafter referred to as ULX-7) was first identified by the Einstein X-ray Observatory in these galaxies (G. G. C. Palumbo et al. 1985). Positioned in a spiral arm to the northwest of the center of NGC 5194, ULX-7 exhibits significant variability. A recent study by G. A. Rodríguez Castillo et al. (2020) determined a spin period of $P_{\rm spin} \approx 2.8$ s and found that the NS was in a 2 day orbit with a $>8M_{\odot}$ companion star, categorizing it as a PULX within a high-mass XRB system. Assuming that variations in the mass accretion rate cause the superorbital modulation, the measured spin-up rate $\dot{P}_{\rm spin} \approx -2.4 \times 10^{-10}$ s s^{-1} indicates a moderately strong magnetic field with $B = 10^{12}$–10^{13} G (G. A. Rodríguez Castillo et al. 2020). Furthermore, C.-P. Hu et al. (2021) and G. Vasilopoulos et al. (2021) also found evidence for periodic dips in the Chandra X-ray light curve that are associated with the 2 day binary orbital period, which suggests an inclination angle of $i \sim 60°$. Recently, M. Imbrogno et al. (2024) detected QPOs at frequencies of ∼0.5 mHz in ULX-7 using three XMM-Newton observations in 2021 and 2022. ;In this study, we conducted a novel phase-resolved analysis of the newly discovered mHz QPOs in ULX-7. We provide an overview of the observations and our data reduction in Section 2, followed by the presentation of the timing and spectral analyses in Section 3. Finally, we discuss and summarize these results in Section 4.

2. Observations and Data Reduction

In this study, we performed a phase-resolved analysis of the mHz QPOs in ULX-7 using data from three XMM-Newton observations (ObsIDs 0883550101, 0883550201, and 0883550301). For convenience, we will refer to these observations as observations 101, 201, and 301, respectively. Details of the XMM-Newton observations utilized in this study can be found in Table 1.

The data were processed using the XMM-Newton SCIENCE ANALYSIS SYSTEM (XMMSAS) version 19.1.0[3] with the latest calibration files (2021 February). The raw data were obtained from the XMM-Newton Science Archive (XSA).[4] We executed the EPPROC and EMPROC tasks to generate the European Photon Imaging Camera PN (EPIC-PN) and Metal Oxide Semi-conductor (EPIC-MOS) event files, respectively. Following the methodology outlined by M. Imbrogno et al. (2024), events were extracted from a circular region with a radius of 20″ centered on the source position (RA = $13^{\rm h}30^{\rm m}01\overset{\rm s}{.}02$, decl. = 47°13′43.″8, J2000; K. D. Kuntz et al. 2016) and were selected to have PATTERN ⩽4 for the EPIC-PN data and PATTERN ⩽12 for the EPIC-MOS data. The background was estimated using an annular region centered on the source position, with inner and outer radii of 21″ and 39″, respectively. To identify periods of high background, we created light curves of the events in the 10–15 keV band. For the timing analysis, we removed only the particle flares at the beginning and/or end of the observation to minimize additional gaps in the light curve. The times of arrival of the photons were corrected to the barycenter of the solar system using the XMMSAS task BARYCEN. Subsequently, the background-corrected light curves for ULX-7 were generated using the EPICLCCORR task. We confirmed that the background flares had no imprint on the background-subtracted light curves, and the source to background flux ratio in the source extraction region during high-background intervals was always higher than 15. Additionally, we examined the timing gaps resulting from the fact that the total count rate exceeded the EPIC-PN and -MOS telemetry limits[5] (∼600 and ∼115 counts s^{-1}, respectively) and found no gaps longer than the time bin size (100 s) used in the timing analysis. For the spectral analysis, we further excluded high-background intervals that occurred during the observations. Response matrices and ancillary response files were created using the XMMSAS tasks RMFGEN and ARFGEN. Finally, the source spectra were grouped using the tool SPECGROUP to apply a minimum of 25 counts per spectral bin and at the same time to not oversample the instrument energy resolution by more than a factor of 3.[6] This allows the application of χ^2 statistics in the spectral modeling.

3. Analysis and Results

3.1. Timing Analysis

We first performed a timing analysis for the three observations. The top panels of Figure 1 present PN+MOS background-subtracted light curves in the 0.3–10 keV energy range, with a time resolution of 2 hr. This resolution was selected to optimize the detection of long-term (≳several hours) flux variability within individual observations, specifically to probe the periodic flux dips reported in previous studies of M51 ULX-7 (C.-P. Hu et al. 2021; G. Vasilopoulos et al. 2021). The 2 hr resolution provides a balance between acceptable statistics and sufficient timing resolution to resolve variability on timescales comparable to the dip durations observed previously (∼8 hr). Three dips are clearly visible in these observations; the dips in observations 101 and 201 are fully observed, whereas the dip in observation 301 appears to be partially seen. To quantitatively characterize the dip features and assess their significance, we employed the Bayesian block[7] technique to identify these dips (J. D. Scargle et al. 2013). With a false alarm probability of $p_0 = 0.005$, we identified four significant flux variations. Three of these variations correspond to visible dips, the edges of which are indicated by black

[3] https://www.cosmos.esa.int/web/XMM-Newton
[4] https://www.cosmos.esa.int/web/XMM-Newton/xsa
[5] https://heasarc.gsfc.nasa.gov/docs/xmm/uhb/epicmode.html
[6] https://heasarc.gsfc.nasa.gov/docs/xmm/sas/help/specgroup/node15.html
[7] https://docs.astropy.org/en/stable/api/astropy.stats.bayesian_blocks.html

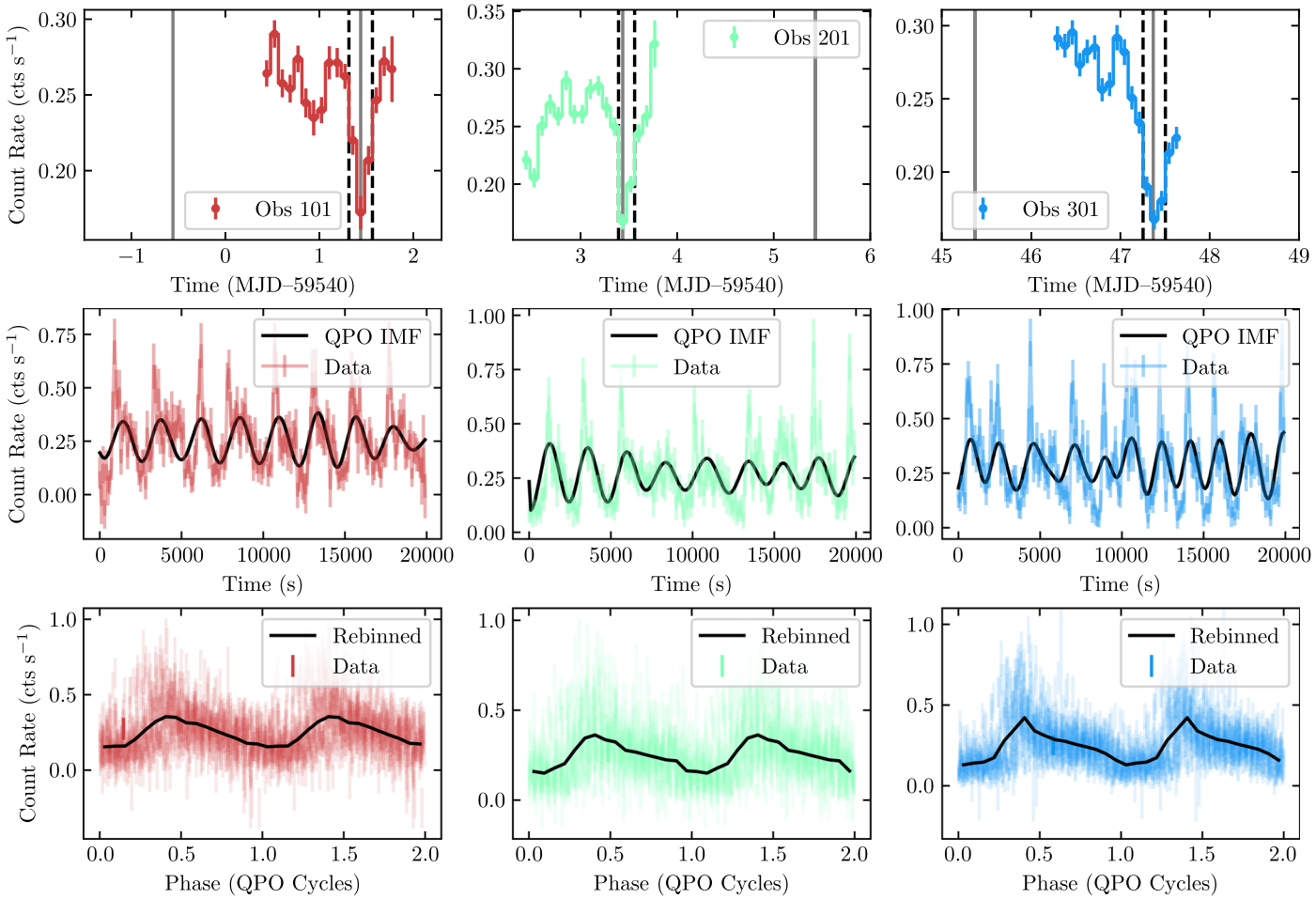

Figure 1. Results of the timing analysis. Top: light curves of M51 ULX-7 with a 2 hr time resolution from the three observations 101, 201, and 301. Black dashed lines indicate the edges of dips obtained from the Bayesian block technique, and gray solid lines indicate the expected arrival times of the dips, assuming the dips occur periodically with an orbital period of 1.9969 days, using the dip time from observation 101 as the reference point. Middle: representative 20 ks light curves (colored points with error bars) with a 100 s time bin from three observations, and the intrinsic QPO light curves (black solid lines) obtained from HHT analysis. Bottom: count rates are plotted against QPO phase as colored points with error bars, and HHT phase-folded light curves are plotted with 20 phase bins per cycle as black solid lines.

dashed lines in the top panels of Figure 1. This suggests that the flux during these dip periods significantly deviates from the long-term flux trend. The central times of the three dips were calculated from the center of the blocks as MJD 59541.44, 59543.48, and 59587.38, respectively. In the top panels of Figure 1, the expected arrival times of the dips are plotted as gray solid lines, assuming the dips occur periodically with an orbital period of 1.9969 days (G. A. Rodríguez Castillo et al. 2020), using the dip time from observation 101 as the reference point. It is evident that the observed dip features occur periodically with each binary orbit. The estimated widths of these dips are 0.23 ± 0.07, 0.22 ± 0.08, and 0.32 ± 0.09 days, consistent with dip features observed by Chandra in 2012 (C.-P. Hu et al. 2021; G. Vasilopoulos et al. 2021). The errors correspond to the standard deviation obtained from bootstrapping. Specifically, bootstrapping involves randomly selecting (with replacement) N times from N bins of data. For our light curves, which consist of 51 time bins, we found that 788 bootstrap iterations were necessary to achieve convergence on the true error distribution.[8] In each bootstrap iteration, we determined the dip widths using the Bayesian block technique. The uncertainties were then estimated as the standard deviations of the width distributions obtained from all bootstrap iterations.

The middle panels of Figure 1 display representative PN +MOS background-subtracted light curves, each covering a period of 20 ks in the 0.3–10 keV energy range, with a time resolution of 100 s. The three light curves exhibit strong, highly structured variability with large amplitudes. The power density spectrum (PDS) can be effectively modeled with several components. One of these components is a Lorentzian function centered at frequencies of $f \sim 0.5$ mHz, with a quality factor $Q = f/\Delta f \sim 2$–10, where Δf is the FWHM of the Lorentzian function (see the Appendix). Consequently, this PDS component is classified as a mHz QPO (see M. Imbrogno et al. 2024 for details). In addition to the mHz QPO, the PDS also exhibits other continuum components, including a broader Lorentzian feature ($Q < 2$) at higher frequencies and a power-law component that dominates at frequencies of $f < 10^{-5}$ Hz. However, in this study, we focus solely on the phase-resolved analysis of the mHz-QPO component. Due to the short timescale ($\sim$10 ks) variations in the recurrence time and amplitude of this QPO variability, period folding for phase-resolved analysis is not suitable. Therefore, we utilized the

[8] Following the $N \cdot (\ln N)^2$ criterion; see E. D. Feigelson & G. Jogesh Babu (2012).

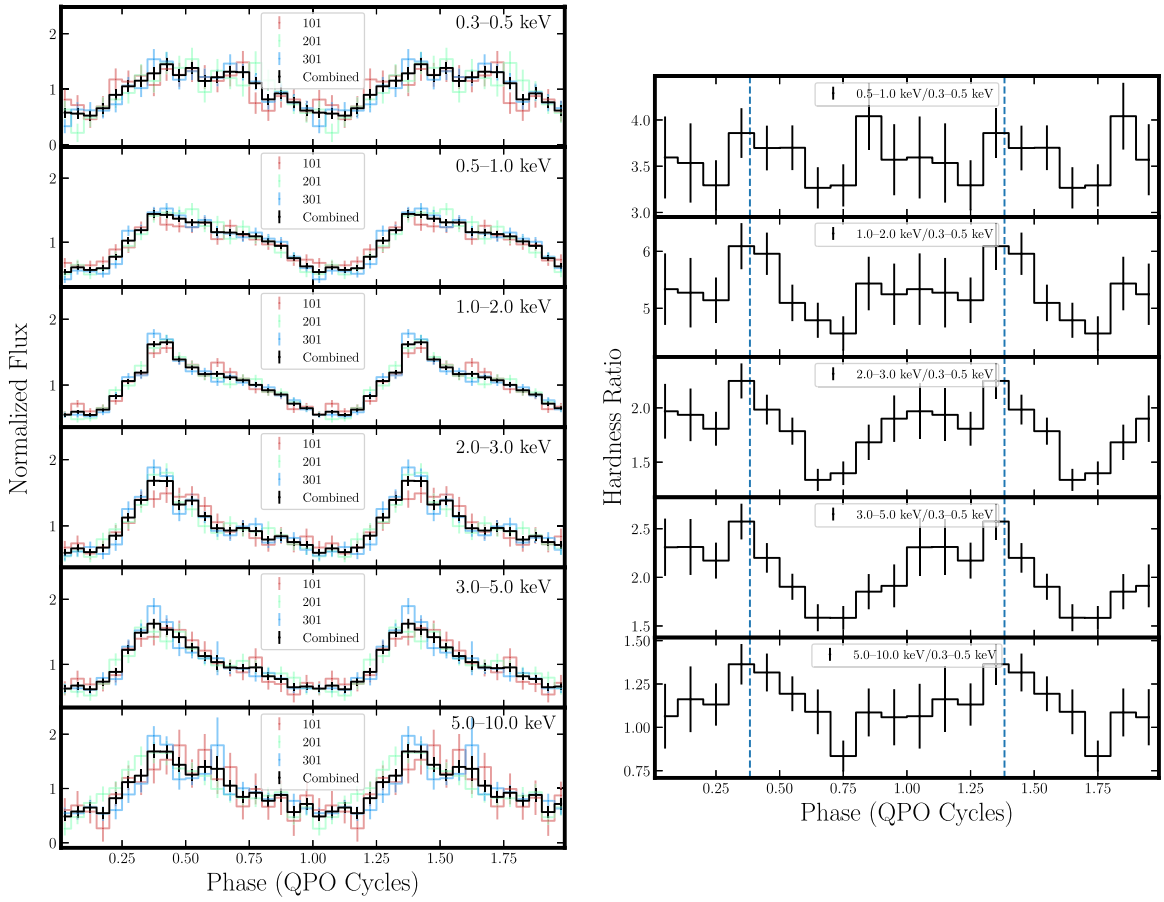

Figure 2. Left: phase-folded light curves for various energy ranges from observations 101 (red), 201 (green), and 301 (blue), and the combined data from all three observations (black). Right: hardness ratios plotted as functions of QPO phase obtained from the combined data. The higher energy bands are defined as follows, from top to bottom: 0.5–1 keV, 1–2 keV, 2–3 keV, 3–5 keV, and 5–10 keV, while the lower energy band is consistently set at 0.3–0.5 keV. The blue dashed lines indicate the peak phases of the folded light curve in the energy range of 0.3–10 keV.

Hilbert–Huang transform (HHT) analysis procedure described by Q. C. Shui et al. (2023) to conduct the phase-resolved analysis of the mHz QPO. The HHT method, originally introduced by N. E. Huang et al. (1998) as an adaptive data analysis technique, serves as a powerful tool for studying signals with nonstationary periodicity (N. E. Huang et al. 1998; N. E. Huang & Z. Wu 2008). This method consists of two main components: mode decomposition and Hilbert spectral analysis (HSA). Mode decomposition can decompose a time series into several intrinsic mode functions (IMFs), while HSA enables the extraction of both the phase function and instantaneous frequency for the desired IMFs, such as QPOs (see, e.g., C.-P. Hu et al. 2014; H.-E. Hsieh & Y. Chou 2020; W. Yu et al. 2023; X. Dai et al. 2024; Q.-C. Shui et al. 2024a; Q.-C. Zhao et al. 2024) and gravitational wave signals (see, e.g., C.-P. Hu et al. 2022; S. Sasaoka et al. 2024). We applied the HHT analysis to the three 100 s time bin PN+MOS background-subtracted light curves within the 0.3–10 keV energy range. By employing variational mode decomposition (K. Dragomiretskiy & D. Zosso 2014), we were able to extract the intrinsic QPO light curves, which are illustrated as solid black lines in the middle panels of Figure 1. Through the application of HSA, we derived the instantaneous phase function of the mHz QPO from each observation. Using these phase functions, the bottom panels of Figure 1 plot the count rate as a function of phase. By rebinning data points into 20 phase bins per cycle, the phase-folded light curves are depicted as solid black lines in the bottom panels of Figure 1. These phase-folded light curves align well with the oscillation features observed in the original light curves and display a nonsinusoidal shape, marked by a rapid ascent followed by a gradual decline.

To study the energy dependence of the mHz QPO, we performed phase folding on light curves across various energy ranges. The left panel of Figure 2 displays the phase-folded light curves for various energy ranges derived from three observations. It is evident that the QPO folding profiles are stable and consistent across the three observations. Therefore, to improve the counting statistics of the folded light curves, we combined the data from the three observations, which are illustrated in black. The modulation of the low-energy ($\lesssim$1 keV) folded light curves maintains a relatively symmetrical appearance, exhibiting an overall morphology that resembles a sinusoidal shape. In contrast, the phase-folded light curves in the higher energy ranges ($\gtrsim$1 keV) show a pronounced nonsinusoidal shape, with a rapid rise in the phases of ∼0–00.4 cycles and a slower decay in the phases of ∼0.4–1 cycles. Overall, the flare (QPO) profiles at lower energies are broader compared to those observed at higher energies. The right panel of Figure 2 plots the hardness ratios as functions of the QPO phase obtained from the combined folded light curves, using 10 phase bins per cycle. The dashed blue lines mark the peak phases of the folded light curve within the energy range of 0.3–10 keV. Significantly, the hardness ratios seem to attain

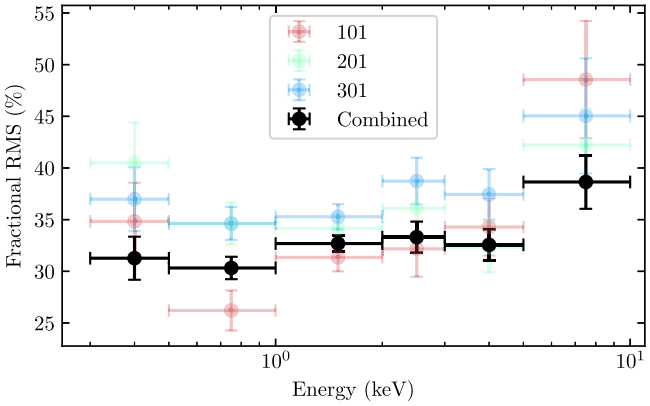

Figure 3. Energy dependence of the fractional rms ($f_{\rm rms}$) of the mHz QPO from observations 101 (red), 201 (green), and 301 (blue), and the combined data from all three observations (black). $f_{\rm rms}$ is computed from Equation (1).

their maximum values at the phases corresponding to the flux peak.

The fractional rms for the mHz-QPO waveform, denoted as $f_{\rm rms}$, was computed for each energy range shown in the left panel of Figure 2. The definition of $f_{\rm rms}$ is given by the following equation:

$$f_{\rm rms} = \frac{\left[\sum_{i=1}^{N}(r_i - \bar{r})^2/N\right]^{1/2}}{\bar{r}}, \quad (1)$$

where $\bar{r}$ is the phase-averaged count rate, r_i is the count rate at the i-th phase bin, and $N = 20$ is the total phase bin number. The energy dependence of $f_{\rm rms}$ is plotted in Figure 3. Despite some slight variations in $f_{\rm rms}$ across different observations, it is evident that the amplitude of the mHz QPO shows an increasing trend over the 0.3–10 keV energy range in each observation. Notably, the rms spectra from observations 101 and 201 exhibit a tentative U-shaped profile, though these trends are not statistically significant.

3.2. Energy Spectral Analysis

Using the well-defined phase functions obtained from the HHT analysis, we extracted EPIC-PN spectra from six distinct phase bins for the three observations, allowing for a subsequent phase-resolved spectral analysis. We conducted the phase-resolved spectral analysis for each observation individually, as well as for the combined data from the three observations, which provided improved counting statistics. The spectral analysis was performed using the XSPEC V12.14.1 software package (K. A. Arnaud 1996). Following M. Brightman et al. (2022) and M. Imbrogno et al. (2024), we modeled the spectra with two absorbed multitemperature disk blackbodies: TBABS × TBABS × (DISKBB+DISKBB). The TBABS model was used to model the interstellar absorption (J. Wilms et al. 2000), with a Milky Way component fixed at $3.3 \times 10^{20}\,{\rm cm}^{-2}$ and a free extragalactic component. To prevent degeneracy in the spectral parameters, we linked the absorption column density of the extragalactic component across the spectra at different phases. By jointly fitting the six phase-resolved spectra with the aforementioned model, we obtained reasonable χ^2/dof values of 234.82/268, 305.64/293, 360.76/347, and 266.15/268 for observations 101, 201, and 301, and combined data from the three observations, respectively. The left panel of Figure 4 illustrates the joint spectral fitting for the combined data, clearly showing that there are no strong features in the residual plots. Additionally, we employed the CFLUX model to calculate the unabsorbed flux contributions from the two DISKBB components. The uncertainties reported for the fitting model parameters represent a 68% confidence range (1σ).

The right panel of Figure 4 illustrates the variability of spectral parameters throughout the mHz-QPO cycle, derived from the joint fitting of the phase-resolved spectra from observations 101 (red), 201 (green), and 301 (blue), and the combined data from all three observations (black) using the aforementioned spectral model. Additionally, the phase-folded light curve of the combined data is included in each panel as a black dashed line. We computed the difference between the maximum and minimum values of each parameter within a cycle to assess the significance of parameter modulation. The results clearly demonstrate that parameters from both DISKBB components exhibit significant variations during the QPO cycle ($>3\sigma$). Notably, the low-temperature component shows significant synchronous changes in disk temperature and flux. The flux modulation of the low-temperature DISKBB component ($F_{\rm disk1}$) is relatively symmetrical, resembling a sinusoidal shape in its overall morphology. In contrast, the flux of the high-temperature component ($F_{\rm disk2}$) exhibits a narrower and more distinctly nonsinusoidal profile. The differing characteristics of the fluxes from the two components align well with the findings presented in the left panel of Figure 2, where the phase-folded light curves across different energy ranges display distinct profiles.

As mentioned above, both of the two disk components exhibit strong variability throughout the QPO cycle. In Figure 5, we illustrate the behavior of these two disk components by plotting their luminosities against their temperatures. To derive the unabsorbed component luminosities, we considered a distance from the source of 8.58 Mpc (K. B. W. McQuinn et al. 2016). For a standard thin disk, the luminosity can be approximated as $L_{\rm disk} \approx 4\pi R_{\rm in}^2 \sigma T_{\rm in}^4$, where $R_{\rm in}$, $T_{\rm in}$, and σ are the inner radius, the temperature, and the Stefan–Boltzmann constant, respectively. In the case of PULXs, the accretion disk is interrupted at the magnetospheric radius $R_{\rm m}$, where the magnetic pressure becomes comparable to the ram pressure of the accreting gas. Inside this radius, the accreting plasma is funneled along the magnetic field lines onto the magnetic poles of the central compact object. The magnetospheric radius can be calculated using the formula

$$R_{\rm m} \approx 7 \times 10^7 \Lambda B_{12}^{4/7} R_6^{10/7} M^{1/7} L_{39}^{-2/7}\,{\rm cm}, \quad (2)$$

where Λ is a parameter that takes into account the geometry of the accretion flow and in the case of an accretion disk is $\approx$0.5, B_{12} is the magnetic dipolar field strength in units of 10^{12} G, R_6 is the NS radius in units of 10^6 cm, M is the NS mass in units of $M_\odot$, and L_{39} is the luminosity in units of $10^{39}\,{\rm erg\,s^{-1}}$. Assuming $R_{\rm in} = R_{\rm m}$ and $L = L_{\rm disk}$, the relationship between the disk luminosity and temperature can be expressed as

$$L_{\rm disk} = 5.8 \times 10^{39} M^{2/11} R_6^{20/11} B_{12}^{8/11} T_{\rm in}^{28/11}\,{\rm erg\,s^{-1}}, \quad (3)$$

where $T_{\rm in}$ is in units of keV, and Λ is assumed to be $\approx$0.5. In Figure 5, we plot the theoretical $L_{\rm disk} \propto T_{\rm in}^4$ and $L_{\rm disk} \propto T_{\rm in}^{28/11}$ relationships as dashed blue and gray lines, respectively, assuming different values for $R_{\rm in}$ and magnetic dipole field strengths. Regarding the low-temperature disk component, within the error range, both theoretical relations can conform to

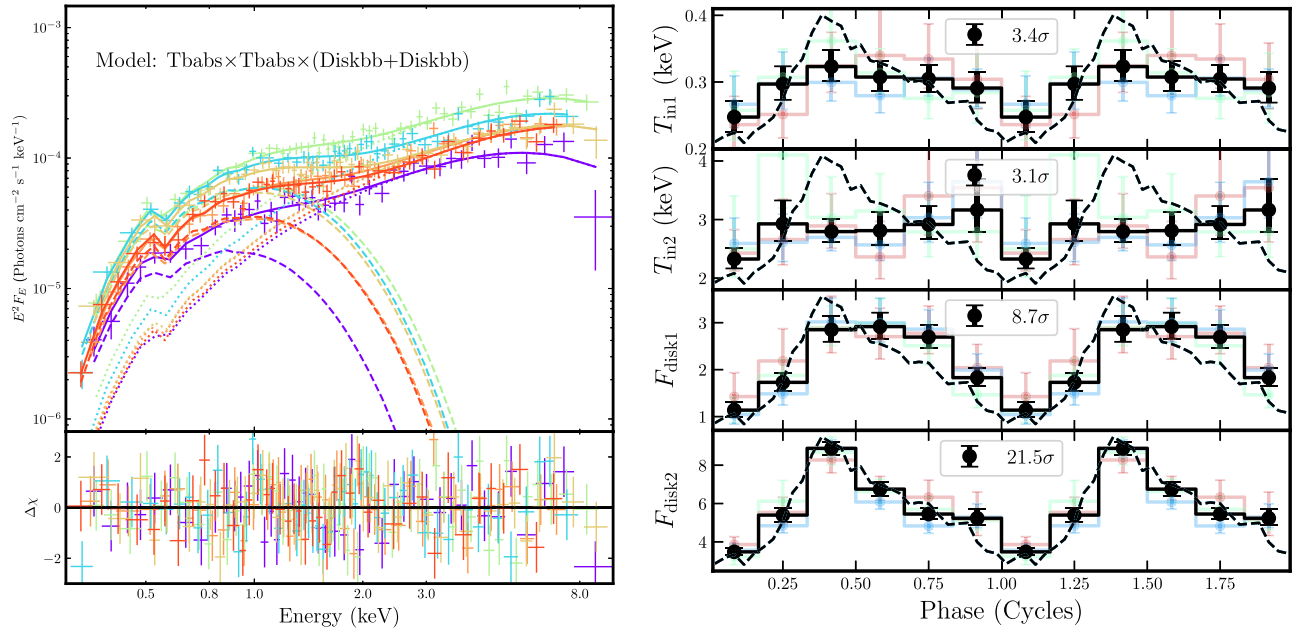

Figure 4. Phase-resolved spectral analyses using model TBABS × TBABS × (DISKBB+DISKBB). Left: joint spectral fittings of the phase-resolved spectra (top panel) and corresponding residual plots (bottom panel) from the combined data of the three observations. Right: variability of spectral parameters during the mHz-QPO cycle obtained from the spectral analyses of observations 101 (red), 201 (green), and 301 (blue), and combined data from the three observations (black). The shown model fluxes ($F_{\rm disk1}$ and $F_{\rm disk2}$) are in units of 10^{-13} erg s^{-1} cm^{-2}. Additionally, the phase-folded light curve is included in each panel as a black dashed line. The statistical significance of each modulation from the combined data is quoted in the corresponding plot.

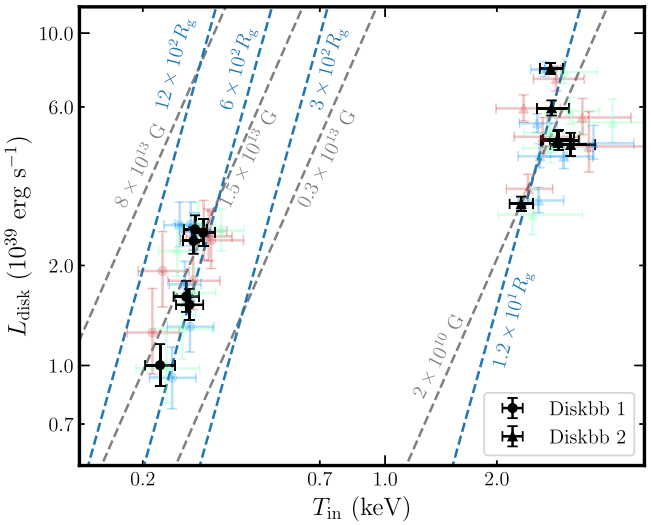

Figure 5. The disk luminosity $L_{\rm disk}$ vs. $T_{\rm in}$ over the mHz-QPO cycle for the low-temperature (circles) and high-temperature (triangles) components from joint fittings of observations 101 (red), 201 (green), and 301 (blue), and combined data from the three observations (black). The dashed blue lines are plotted assuming $L_{\rm disk} = 4\pi\sigma R_{\rm in}^2 T_{\rm in}^4$, where $R_{\rm in}$ remains constant over the QPO cycle. The dashed gray lines are plotted assuming $R_{\rm in} = R_{\rm m}$ over the QPO cycle.

the data points. If we assume that the inner radius does not change during the QPO cycle, it can be approximated as $\sim 600 R_{\rm g} \approx 1.2 \times 10^8$ cm, where M is assumed to be $1.4 M_\odot$. Taking into account $R_{\rm in} = R_{\rm m}$, the magnetic field strength can be estimated at $\sim 1.5 \times 10^{13}$ G, which is consistent with previous estimates ($\sim 10^{12}$–10^{13} G, G. A. Rodríguez Castillo et al. 2020; G. Vasilopoulos et al. 2021). In contrast, the data points for the high-temperature disk component show significant deviations from the two theoretical relationships.

4. Discussion and Conclusion

This study has conducted a comprehensive phase-resolved analysis of ∼0.5 mHz QPOs in M51 ULX-7. Previous theoretical studies have proposed that mHz QPOs and day timescale periods/QPOs (e.g., superorbital modulation) are associated with Lense–Thirring precession of the inflow and outflowing wind, respectively (M. J. Middleton et al. 2018, 2019). In this Lense–Thirring scenario, variability of X-ray mHz QPOs arises from the geometric wobble of the accretion disk, which alters the projection area of the disk relative to the observer, thereby modulating the observed X-ray flux (A. Ingram et al. 2009). This leads to the expectation that the temperature of the disk would not be modulated in sync with the QPO cycle. Contrary to this expectation, our phase-resolved analysis revealed significant variations in spectral shape, particularly demonstrating synchronous variations in disk temperature and flux. Furthermore, if the Lense–Thirring scenario is indeed applicable, precession should primarily occur within the spherization radius $R_{\rm sph}$ (M. J. Middleton et al. 2018), where the radiation force from the energy released in the disk is no longer balanced by gravity, causing the disk to become geometrically thick and launch powerful outflows (N. I. Shakura & R. A. Sunyaev 1973). Under this assumption, if the low-temperature component originates from a region outside of $R_{\rm sph}$, it would not be expected to exhibit modulation with the QPO phase. However, our findings indicate that both disk components display significant modulations throughout the QPO cycle. Thus, we conclude that existing models of the Lense–Thirring scenario do not adequately account for our results, suggesting the need for further exploration and refinement of theoretical frameworks to explain the observed phenomena in this system.

An alternative possibility is that the mHz QPOs arise from limit-cycle instabilities within the accretion disk, driven by the radiation pressure instability (A. P. Lightman & D. M. Eardley 1974;

E. Szuszkiewicz & J. C. Miller 1998; A. Janiuk et al. 2000). This mechanism has been extensively considered as the potential origin of the class ρ "heartbeat" variability observed in GRS 1915+105 (T. Belloni et al. 2000). We found that the mHz-QPO waveform in the 0.3–10 keV energy range exhibits a nonsinusoidal feature, characterized by a fast rise and slow decay. This pattern contrasts with the class ρ "heartbeat" variability, which displays a slow rise followed by a rapid decay (J. Neilsen et al. 2011). Furthermore, the class ρ "heartbeat" variability is characterized by a more stable variability pattern than the one seen in the ULX-7 light curves. Notably, the flux modulation shape we observed in ULX-7 is similar to that of Class X "heartbeat"-like variability seen in IGR J17091–3624 (Q.-C. Shui et al. 2024b; J. Wang et al. 2024). Additionally, both variability patterns exhibit synchronous variations in the temperature and flux of the low-temperature disk component. Therefore, the observed mHz QPOs, akin to Class X "heartbeat"-like variability in IGR J17091–3624, could originate from instabilities within the accretion disk, resulting in quasiperiodic fluctuations in the accretion rate.

By plotting $L_{\rm disk}$ against $T_{\rm in}$ throughout the QPO cycle for both disk components and comparing the data points with theoretical relations, we demonstrated that the low-temperature component in the spectrum from M51 ULX-7 originates from an accretion disk truncated at the magnetospheric radius $R_{\rm m}$, rather than from outflowing winds. This conclusion is supported by the fact that if the low-temperature component was associated with outflowing winds, one would not expect a positive correlation between luminosity and temperature (J. J. E. Kajava & J. Poutanen 2009; R. Soria & A. Kong 2016; A. King et al. 2023). Assuming that the inner radius of the low-temperature disk is equal to $R_{\rm m}$, the inferred magnetic field strength is $\sim 1.5 \times 10^{13}$ G, which is consistent with previous estimates ($\sim 10^{12}$–10^{13} G, G. A. Rodríguez Castillo et al. 2020; G. Vasilopoulos et al. 2021).

Since the low-temperature disk component originates from the magnetically truncated outer disk, its luminosity variability roughly reflects fluctuations in the accretion rate, particularly if the X-ray mHz-QPO variability is driven by the accretion rate variations. Consequently, the modulation of the accretion rate throughout the QPO phase mirrors that of the low-energy flux, resembling a roughly sinusoidal shape (see Figure 2). The high-temperature component may originate from the accretion curtain (A. A. Mushtukov et al. 2017) and/or the inner thick accretion disk ($R < R_{\rm sph}$). The accretion curtain is a magnetically confined, optically thick structure that channels material from the inner accretion disk to the magnetic poles of the central compact object. In these regions, strong, optically thick outflowing winds are effectively launched from the accretion flow, forming a funnel-like structure (see, e.g., J. Poutanen et al. 2007; K. Ohsuga & S. Mineshige 2011; Y.-F. Jiang et al. 2014; A. A. Mushtukov et al. 2019). This geometrical configuration is expected to result in beaming of the hard X-ray emissions from the funnel. Therefore, the beaming effect could potentially amplify high-energy variability and render the high-energy QPO waveform narrower in comparison to the low-energy one (see Figures 2 and 3). Additionally, there may be an accretion rate dependence of the beaming factor, expressed as $b \propto \dot{m}^{-2}$ (A. R. King 2009), which could further enhance the amplitude of high-energy variability. Given that the high-energy variability exhibits a greater amplitude than the low-energy variability, we would expect the hardness ratio to be higher during the peak phases of the variability cycle. The tentative U-shaped feature in rms spectra of observations 101 and 201, however, remains inconclusive due to limited photon statistics; future advanced missions like eXTP (S. Zhang et al. 2019) and Athena (K. Nandra et al. 2013) will be critical to confirm its physical origin.

The relatively longer exposure times of the three XMM-Newton observations compared to previous observations allow us to robustly detect three periodic flux dips. These dips are likely recurrent, with a period of approximately 2 days, which is consistent with the orbital period of M51 ULX-7 (G. A. Rodríguez Castillo et al. 2020). The estimated widths of these dips are approximately ~0.15–0.4 days, aligning with the dip features observed by Chandra in 2012 (C.-P. Hu et al. 2021; G. Vasilopoulos et al. 2021). Given the similarities in the properties of the dip features observed by XMM-Newton and Chandra, we propose that they share the same origin, which is related to the binary orbital period. Since the total eclipse was not observed, C.-P. Hu et al. (2021) suggested that the periodic dips result from obscuration of the emission from the accreting pulsar due to the vertical structure in the stream–disk interaction region or the atmosphere of the companion star.

Acknowledgments

We are grateful to the anonymous referee for constructive comments that helped us improve this paper. This research has made use of data obtained from the High Energy Astrophysics Science Archive Research Center (HEASARC), provided by NASA's Goddard Space Flight Center. This work is supported by the National Key R&D Program of China (2021YFA0718500) and the National Natural Science Foundation of China (NSFC) under grants 12025301 and 12333007. This work is partially supported by the International Partnership Program of the Chinese Academy of Sciences (grant No. 113111KYSB20190020).

Appendix
Power Density Spectrum Analysis

The PDSs of the three observations of M51 ULX-7 were constructed and modeled following the procedure described by M. Imbrogno et al. (2024). The 0.3–10 keV PDSs were computed with a bin time of 5 s in 1 segment, resulting in the minimum and Nyquist frequencies of $\sim 6 \times 10^{-6}$ and 0.1 Hz, respectively. The PDSs were then logarithmically rebinned in frequency with a bin size increasing by a factor of 1.2 and normalized to units of fractional rms squared per Hz (T. Belloni & G. Hasinger 1990). We fitted the PDSs with a model containing two Lorentzian components, a power-law component, and a constant component (see Equation (1) of M. Imbrogno et al. 2024). The two Lorentzians describe the broad shoulder at higher frequencies and the mHz QPO at lower frequencies, while the power-law component models the red noise dominant at frequencies $f < 10^{-5}$ Hz. The constant component accounts for the white noise. Our fitting results are consistent with those presented in Table 2 of M. Imbrogno et al. (2024). Figure A1 shows the PDS analysis of observation 101 as an example, with the Poisson noise (derived from the best-fit constant component) subtracted.

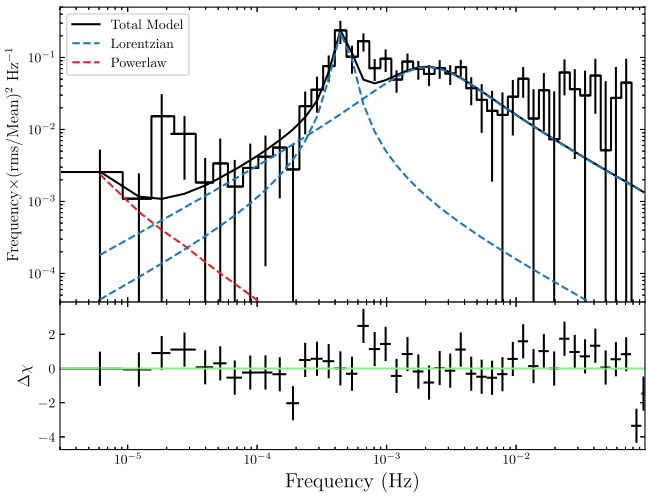

Figure A1. A PDS analysis of observation 101. Top panel: 0.3–10 keV Poisson-noise-subtracted PDS fitted with a model (solid black line) consisting of two Lorentzian components (dashed blue lines) and a power-law (dashed red line) component. Bottom panel: residuals of the PDS with respect to the derived model.

ORCID iDs

Qing-Cang Shui https://orcid.org/0000-0001-5160-3344
Hua Feng https://orcid.org/0000-0001-7584-6236
Yu-Peng Chen https://orcid.org/0000-0001-8768-3294
Shuang-Nan Zhang https://orcid.org/0000-0001-5586-1017
Jing-Qiang Peng https://orcid.org/0000-0002-5554-1088

References

Agrawal, V. K., & Nandi, A. 2015, MNRAS, 446, 3926
Arnaud, K. A. 1996, in ASP Conf. Ser. 101, Astronomical Data Analysis Software and Systems V, ed. G. H. Jacoby & J. Barnes (San Francisco, CA: ASP), 17
Bachetti, M., Harrison, F. A., Walton, D. J., et al. 2014, Natur, 514, 202
Belloni, T., & Hasinger, G. 1990, A&A, 230, 103
Belloni, T., Klein-Wolt, M., Méndez, M., van der Klis, M., & van Paradijs, J. 2000, A&A, 355, 271
Brightman, M., Bachetti, M., Earnshaw, H., et al. 2022, ApJ, 925, 18
Dai, X., Kong, L., Ji, L., et al. 2024, A&A, 692, A117
Dall'Osso, S., Perna, R., & Stella, L. 2015, MNRAS, 449, 2144
Dewangan, G. C., Griffiths, R. E., & Rao, A. R. 2006, ApJL, 641, L125
Dragomiretskiy, K., & Zosso, D. 2014, ITSP, 62, 531
Feigelson, E. D., & Jogesh Babu, G. 2012, Modern Statistical Methods for Astronomy (Cambridge: Cambridge Univ. Press)
Feng, H., Rao, F., & Kaaret, P. 2010, ApJL, 710, L137
Feng, H., & Soria, R. 2011, NewAR, 55, 166
Hsieh, H.-E., & Chou, Y. 2020, ApJ, 900, 116
Hu, C.-P., Chou, Y., Yang, T.-C., & Su, Y.-H. 2014, ApJ, 788, 31
Hu, C.-P., Lin, L. C.-C., Pan, K.-C., et al. 2022, ApJ, 935, 127
Hu, C.-P., Ueda, Y., & Enoto, T. 2021, ApJ, 909, 5
Huang, N. E., Shen, Z., Long, S. R., et al. 1998, RSPSA, 454, 903
Huang, N. E., & Wu, Z. 2008, RvGeo, 46, RG2006
Imbrogno, M., Motta, S. E., Amato, R., et al. 2024, A&A, 689, A284
Ingram, A., Done, C., & Fragile, P. C. 2009, MNRAS, 397, L101
Ingram, A. R., & Motta, S. E. 2019, NewAR, 85, 101524
Janiuk, A., Czerny, B., & Siemiginowska, A. 2000, ApJL, 542, L33
Jiang, Y.-F., Stone, J. M., & Davis, S. W. 2014, ApJ, 796, 106
Kaaret, P., Feng, H., & Roberts, T. P. 2017, ARA&A, 55, 303
Kajava, J. J. E., & Poutanen, J. 2009, MNRAS, 398, 1450
King, A., Lasota, J.-P., & Kluźniak, W. 2017, MNRAS, 468, L59
King, A., Lasota, J.-P., & Middleton, M. 2023, NewAR, 96, 101672
King, A. R. 2009, MNRAS, 393, L41
Kosec, P., Pinto, C., Fabian, A. C., & Walton, D. J. 2018a, MNRAS, 473, 5680
Kosec, P., Pinto, C., Walton, D. J., et al. 2018b, MNRAS, 479, 3978
Kuntz, K. D., Long, K. S., & Kilgard, R. E. 2016, ApJ, 827, 46
Lightman, A. P., & Eardley, D. M. 1974, ApJL, 187, L1
Lipunova, G. V. 1999, AstL, 25, 508
McQuinn, K. B. W., Skillman, E. D., Dolphin, A. E., Berg, D., & Kennicutt, R. 2016, ApJ, 826, 21
Middleton, M. J., Fragile, P. C., Bachetti, M., et al. 2018, MNRAS, 475, 154
Middleton, M. J., Fragile, P. C., Ingram, A., & Roberts, T. P. 2019, MNRAS, 489, 282
Middleton, M. J., & King, A. 2017, MNRAS, 470, L69
Motta, S. E., Marelli, M., Pintore, F., et al. 2020, ApJ, 898, 174
Mushtukov, A. A., Ingram, A., Middleton, M., Nagirner, D. I., & van der Klis, M. 2019, MNRAS, 484, 687
Mushtukov, A. A., Portegies Zwart, S., Tsygankov, S. S., Nagirner, D. I., & Poutanen, J. 2021, MNRAS, 501, 2424
Mushtukov, A. A., Suleimanov, V. F., Tsygankov, S. S., & Ingram, A. 2017, MNRAS, 467, 1202
Nandra, K., Barret, D., Barcons, X., et al. 2013, arXiv:1306.2307
Nayakshin, S., Rappaport, S., & Melia, F. 2000, ApJ, 535, 798
Neilsen, J., Remillard, R. A., & Lee, J. C. 2011, ApJ, 737, 69
Ohsuga, K., & Mineshige, S. 2011, ApJ, 736, 2
Palumbo, G. G. C., Fabbiano, G., Fransson, C., & Trinchieri, G. 1985, ApJ, 298, 259
Pasham, D. R., Strohmayer, T. E., & Mushotzky, R. F. 2014, Natur, 513, 74
Pinto, C., Middleton, M. J., & Fabian, A. C. 2016, Natur, 533, 64
Pinto, C., Walton, D. J., Kara, E., et al. 2020, MNRAS, 492, 4646
Poutanen, J., Lipunova, G., Fabrika, S., Butkevich, A. G., & Abolmasov, P. 2007, MNRAS, 377, 1187
Rao, F., Feng, H., & Kaaret, P. 2010, ApJ, 722, 620
Rodríguez Castillo, G. A., Israel, G. L., Belfiore, A., et al. 2020, ApJ, 895, 60
Sasaoka, S., Sakai, Y., Dominguez, D., et al. 2024, PhRvD, 110, 104020
Scargle, J. D., Norris, J. P., Jackson, B., & Chiang, J. 2013, ApJ, 764, 167
Shakura, N. I., & Sunyaev, R. A. 1973, A&A, 24, 337
Shui, Q.-C., Zhang, S., Peng, J.-Q., et al. 2024a, ApJ, 973, 59
Shui, Q.-C., Zhang, S., Peng, J.-Q., et al. 2024b, ApJ, 973, 92
Shui, Q. C., Zhang, S., Zhang, S. N., et al. 2023, ApJ, 957, 84
Soria, R., & Kong, A. 2016, MNRAS, 456, 1837
Strohmayer, T. E., & Mushotzky, R. F. 2003, ApJL, 586, L61
Strohmayer, T. E., Mushotzky, R. F., Winter, L., et al. 2007, ApJ, 660, 580
Szuszkiewicz, E., & Miller, J. C. 1998, MNRAS, 298, 888
Tranin, H., Webb, N., Godet, O., & Quintin, E. 2024, A&A, 681, A16
Urquhart, R. T., Soria, R., Di Stefano, R., et al. 2022, MNRAS, 511, 4528
Vasilopoulos, G., Koliopanos, F., Haberl, F., et al. 2021, ApJ, 909, 50
Walton, D. J., Mackenzie, A. D. A., Gully, H., et al. 2022, MNRAS, 509, 1587
Wang, J., Kara, E., Garcìa, J. A., et al. 2024, ApJ, 963, 14
Wilms, J., Allen, A., & McCray, R. 2000, ApJ, 542, 914
Yu, W., Bu, Q.-C., Yang, Z.-X., et al. 2023, ApJ, 951, 130
Zhang, S., Santangelo, A., Feroci, M., et al. 2019, SCPMA, 62, 29502
Zhao, Q.-C., Tao, L., Li, H.-C., et al. 2024, ApJL, 961, L42